Available online at www.sciencedirect.com
ScienceDirect
Journal of Computational Physics 227 (2008) 7003–7026
JOURNAL OF COMPUTATIONAL PHYSICS
www.elsevier.com/locate/jcp

Stability and convergence of the method of fundamental solutions for Helmholtz problems on analytic domains

A.H. Barnett [a,*], T. Betcke [b]

[a] Department of Mathematics, 6188 Kemeny Hall, Dartmouth College, Hanover, NH 03755, USA
[b] School of Mathematics, The University of Manchester, Manchester M13 9PL, UK

Received 26 August 2007; received in revised form 21 March 2008; accepted 3 April 2008
Available online 20 April 2008

Abstract

The method of fundamental solutions (MFS) is a popular tool to solve Laplace and Helmholtz boundary value problems. Its main drawback is that it often leads to ill-conditioned systems of equations. In this paper, we investigate for the interior Helmholtz problem on analytic domains how the singularities (charge points) of the MFS basis functions have to be chosen such that approximate solutions can be represented by the MFS basis in a numerically stable way. For Helmholtz problems on the unit disc we give a full analysis which includes the high frequency (short wavelength) limit. For more difficult and nonconvex domains such as crescents we demonstrate how the right choice of charge points is connected to how far into the complex plane the solution of the boundary value problem can be analytically continued, which in turn depends on both domain shape and boundary data. Using this we develop a recipe for locating charge points which allows us to reach error norms of typically 10^{-11} on a wide variety of analytic domains. At high frequencies of order only 3 points per wavelength are needed, which compares very favorably to boundary integral methods.

MSC: 65N12; 65N35; 78M25

Keywords: Helmholtz equation; Boundary value problem; Method of fundamental solutions; Analytic continuation; High frequency waves

1. Introduction

The method of fundamental solutions (MFS), also known as the charge simulation method or the method of auxiliary sources, is a well known method for solving Laplace or Helmholtz boundary value problems

* Corresponding author. Tel.: +1 603 646 3178; fax: +1 603 646 1312.
E-mail addresses: ahb@math.dartmouth.edu (A.H. Barnett), timo.betcke@manchester.ac.uk (T. Betcke).
URLs: http://www.math.dartmouth.edu/~ahb (A.H. Barnett), http://www.maths.man.ac.uk/~tbetcke (T. Betcke).

0021-9991/$ - see front matter © 2008 Elsevier Inc. All rights reserved.
doi:10.1016/j.jcp.2008.04.008

(BVPs). The idea is to approximate the solution by fundamental solutions of the Laplace or Helmholtz equation whose singularities lie outside the domain. Consider the boundary value problem

$$\Delta u + k^2 u = 0 \quad \text{in } \Omega, \tag{1a}$$

$$u = v \quad \text{on } \partial\Omega, \tag{1b}$$

where $\Omega \subset \mathbb{R}^2 = \mathbb{C}$ is a simply connected planar domain with analytic boundary $\partial\Omega$. This means that there exists a parameterization of $\partial\Omega$ in the form of an analytic function $Z(s)$ for $s \in [0, 2\pi]$, with $Z(0) = Z(2\pi)$. For simplicity we will often equivalently say that Ω is analytic. We call the boundary data v analytic if $v(s)$ is a 2π-periodic analytic function.

Recall that the solution is unique if and only if k^2 is not a Dirichlet eigenvalue (of the Laplacian) for the domain; physically this is a resonance effect. The idea of the MFS is to approximate u by a linear combination of fundamental solutions of the form

$$u(\mathbf{x}) \approx u^{(N)}(\mathbf{x}) = \frac{i}{4} \sum_{j=1}^{N} \alpha_j H_0^{(1)}(k|\mathbf{x} - \mathbf{y}_j|), \quad \mathbf{y}_j \in \mathbb{R}^2 \setminus \overline{\Omega}, \tag{2}$$

where $H_0^{(1)} = J_0 + iY_0$ is a Hankel function of the first kind of order zero, J_0 is a Bessel function of the first kind of order zero and Y_0 is a Bessel function of the second-kind of order zero. N is the number of approximating functions each of which is associated with a charge point $\mathbf{y}_j$. It is well known that $H_0^{(1)}$ satisfies the Helmholtz equation in $\mathbb{C} \setminus \{0\}$ with a singularity at zero. It is common to choose charge points lying on a smooth curve; we then may interpret the MFS as a discretization of the following external single layer potential representation of u. Let Γ be a closed curve enclosing $\overline{\Omega}$ such that $\operatorname{dist}(\Gamma, \partial\Omega) := \min\{|\mathbf{x} - \mathbf{y}|, \mathbf{x} \in \partial\Omega, \mathbf{y} \in \Gamma\} > 0$, then given a density $g \in L^1(\Gamma)$ we may write

$$u(\mathbf{x}) \approx \frac{i}{4} \int_{\Gamma} H_0^{(1)}(k|\mathbf{x} - \mathbf{s}|) g(\mathbf{s}) \mathrm{d}\mathbf{s}, \quad \mathbf{x} \in \Omega. \tag{3}$$

If $g(\mathbf{s}) = \sum_{j=1}^{N} \alpha_j \delta(\mathbf{s} - \mathbf{y}_j)$ for some point set $\{\mathbf{y}_j\} \in \Gamma$, where δ is the Dirac delta, we recover the MFS formulation (2). Note that Y_0 or $H_0^{(2)}$ may be used instead of $H_0^{(1)}$ in the MFS [10,13]; see Remark 1 below.

An overview of the history of the method and its applications, which have largely been in the engineering community, is given in [11]. The rate of convergence of the MFS for the Laplace ($k = 0$) BVP was investigated in [4,15–18]. It turns out that if the boundary data is analytic one can achieve exponential convergence for the MFS for the Laplace problem on analytic domains if the charge points $\mathbf{y}_j$ are suitably chosen. The MFS differs from the common approach of discretizing boundary integral equations (BIE) [5] in that, since Γ is separated from $\partial\Omega$, there is no jump relation nor singularity of the kernel. Thus one advantage over BIE is that the solution may be simply and accurately evaluated up to the boundary. There appear to be few performance comparisons of MFS against BIE in the literature [2]; our goal in this work is not to undertake such a task, but we will show that MFS may be competitive and hence deserves analysis.

One of the main drawbacks of MFS is that (unlike with second-kind BIE) systems of equations or linear least-squares problems have to be solved that are ill-conditioned. This feature is shared by Radial Basis Functions [9]. The effects of this ill-conditioning on the quality of the MFS solution have been investigated for the Laplace case in [20,21]. In this paper, we investigate more closely for the Helmholtz problem the conditions on the charge points $\mathbf{y}_j$ which lead to a numerically stable representation of an approximate solution. It turns out that this depends on how far into the complex plane a solution of (1a) can be analytically continued. The importance of this in the context of scattering problems has already been observed [23,24,8].

Our work also has consequences for the efficient numerical solution of related more challenging and widely applicable PDE problems. We have in mind (i) finding eigenmodes of the Laplace operator in Ω with homogeneous boundary conditions (where the MFS has been used at low [10] and very high eigenvalue [3]) and (ii) scattering of time-harmonic waves (the exterior Helmholtz boundary value problem in $\mathbb{R}^2 \setminus \overline{\Omega}$). In both these situations the boundary data is almost always analytic: in problem (i) it is zero and in (ii) a plane wave or point source.

We will study convergence of the MFS approximation in the boundary error norm

$$t = \|u^{(N)} - v\|_{L^2(\partial\Omega)}. \tag{4}$$

By applying [22, Eq. (7)], this controls the interior error of the solution as follows:

$$\|u^{(N)} - u\|_{L^2(\Omega)} \leqslant \frac{C_\Omega}{d}\|u^{(N)} - v\|_{L^2(\partial\Omega)}, \tag{5}$$

where $d := \min_j |k^2 - E_j|/E_j$, the domain's Dirichlet eigenvalues are E_j, and C_Ω is a domain-dependent constant. This shows that for any fixed nonresonant k, we may use the boundary norm.

In Section 2 we give rigorous results for the convergence and the numerical stability of the MFS for Helmholtz problems on the unit disc, with analytic boundary data, using charge points on a concentric circle. We then present a heuristic model for behavior in finite-precision arithmetic and show it explains well numerical results observed at both low and high wavenumbers. A key conclusion will be that it is the growth in norm of the coefficient vector that in practice limits the achievable error, so this norm should be kept as small as possible to retain high accuracy. The reader should take care throughout not to confuse statements about the *coefficient norm* (which depending on the choice of MFS charge points may either grow or not grow with N as the error converges to zero), with statements about the *condition number* of the problem (which always grows with N since the MFS (2) approximates a single layer operator (3) which is compact).

In Section 3.1 we move to general analytic domains, and review results for the analytic continuation of solutions u of (1a), in particular how both the boundary data and the domain shape may lead to singularities in the continuation of u. Exterior conformal maps play an important theoretical role in the analysis of the MFS for Laplace problems [17], thus in Section 3.2 we explore the use of such maps to choose charge points for Helmholtz problems in several challenging domains. We propose and provide evidence for conjectures in general domains analogous to our theorems on convergence rate and stability in the unit disc. For nonconvex domains charge points determined by exterior conformal maps can lead to bad results. This motivates a heuristic conformally related method proposed in Section 3.3, which circumvents this problem and in Section 3.4 is shown to be an efficient representation in the high frequency (large k) limit.

2. The MFS on the unit disc

In this section, we analyse the accuracy and coefficient sizes that result in the unit disc $\Omega = \{\mathbf{x} : |\mathbf{x}| < 1\}$, for the MFS using charge points $\mathbf{y}_j = Re^{i\phi_j}$, $j = 1, 2, \ldots, N$, with $\phi_j = 2\pi j/N$, that is, equally spaced on a larger circle of radius $R > 1$ (see Fig. 1).

Before we embark we need to define the Fourier series of a function $g \in L^2([0, 2\pi])$,

$$g(\theta) = \sum_{m=-\infty}^{\infty} \hat{g}(m)e^{im\theta}, \quad \hat{g}(m) = \frac{1}{2\pi}\int_0^{2\pi} g(\theta)e^{-im\theta}\,d\theta. \tag{6}$$

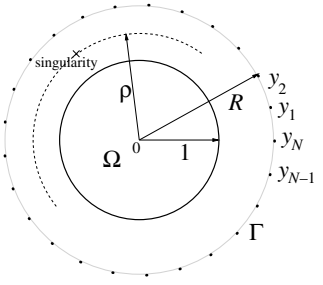

Fig. 1. Geometry for the MFS in the unit disc.

Parseval's identity is then

$$\|g\|^2_{L^2([0,2\pi])} = 2\pi \sum_{m=-\infty}^{\infty} |\hat{g}(m)|^2 =: 2\pi \|\hat{g}\|^2_{\ell^2(\mathbb{Z})}. \tag{7}$$

We also need to represent the coefficient vector $\boldsymbol{\alpha} := \{\alpha_j\}_{j=1,\ldots,N}$ in a discrete Fourier basis labeled by $-N/2 < k \leqslant N/2$ (we will always choose N even),

$$\alpha_j = \sum_{k=-N/2+1}^{N/2} \hat{\alpha}_k e^{ik\phi_j}, \quad \hat{\alpha}_k = \frac{1}{N} \sum_{j=1}^{N} \alpha_j e^{-ik\phi_j}, \tag{8}$$

where inversion follows from $\sum_{j=1}^{N} e^{2\pi i k j/N} = N\delta^{(N)}_{k0}$, with $\delta^{(N)}_{k0}$ the periodized Kronecker delta defined by

$$\delta^{(N)}_{kj} = \begin{cases} 1, & k \equiv j \pmod N \\ 0, & \text{otherwise.} \end{cases} \tag{9}$$

Parseval's identity now gives $|\boldsymbol{\alpha}|^2 = N|\hat{\boldsymbol{\alpha}}|^2$, where $|\boldsymbol{\alpha}| := (|\alpha_1|^2 + \cdots + |\alpha_n|^2)^{1/2}$ is the standard Euclidean norm.

2.1. Map from layer potential to Fourier basis on the unit circle

For simplicity we first consider the layer potential version of the problem, which can be interpreted as the $N \to \infty$ limit of the MFS. The single layer potential lying on the outer circle $\Gamma = \{\mathbf{y} : |\mathbf{y}| = R\}$ is

$$u(\mathbf{x}) = \frac{i}{4} \int_0^{2\pi} H_0^{(1)}(k|\mathbf{x} - Re^{i\phi}|) g(\phi) d\phi. \tag{10}$$

Note $g \in L^1([0, 2\pi])$ is the density with respect to angle measure $d\phi$ rather than the usual length measure $Rd\phi$. The Fourier–Bessel decomposition of a fundamental solution located at $Re^{i\phi}$, evaluated at $\mathbf{x} = Re^{i\theta}$ is, using Graf's addition formula [1, Eq. (9.1.79)],

$$\frac{i}{4} H_0^{(1)}(k|\mathbf{x} - Re^{i\phi}|) = \frac{i}{4} \sum_{m\in\mathbb{Z}} H_m^{(1)}(kR) J_m(kr) \cos m(\theta - \phi) = \frac{i}{4} \sum_{m\in\mathbb{Z}} H_m^{(1)}(kR) e^{-im\phi} \cdot J_m(kr) e^{im\theta} \tag{11}$$

where the second step involved the reflection formulae [1, Eq. (9.1.5)] $J_{-m}(z) = (-1)^m J_m(z)$ and $Y_{-m}(z) = (-1)^m Y_m(z)$. Hence the Fourier–Bessel coefficients are $\frac{i}{4} H_m^{(1)}(kR) e^{-im\phi}$. The restriction of (10) to $\mathbf{x} \in \partial\Omega$ gives a single layer operator $S : L^2([0, 2\pi]) \to L^2([0, 2\pi])$ of convolution type, which is therefore diagonal in the Fourier basis $\{e^{im\theta}\}_{m\in\mathbb{Z}}$ and entirely described by its eigenvalues. Comparing (10) and (11) and using orthogonality gives $\hat{u}(m) = \hat{s}(m)\hat{g}(m)$ where the eigenvalues of S are

$$\hat{s}(m) = \frac{i\pi}{2} H_m^{(1)}(kR) J_m(k). \tag{12}$$

Remark 1. Since the Hankel function (of real argument) is never zero, an eigenvalue can vanish only when $J_m(k) = 0$, corresponding to a Dirichlet eigenvalue (resonance) of Ω. In contrast if Y_0 were chosen as the fundamental solution in (2), $Y_m(kR)$ may accidentally be very small giving poor or spurious numerical results, although in practice this happens rarely [10]. In general one may avoid this problem by using $(Y_0 + i\eta J_0)$ for any η with $\mathrm{Re}\ \eta \neq 0$ (an analogous idea is used in layer potentials [5, p. 48]).

Since its kernel is continuous S is compact, so $\lim_{|m|\to\infty} \hat{s}(m) = 0$, S^{-1} is unbounded, and we expect arbitrarily large $\|g\|$ will be needed to represent certain unit-norm boundary functions v.

In the Laplace ($k \to 0$) limit we recover the following known result (e.g. [16, Eq (3.2)]). We use the small-argument asymptotics $J_m(k) \sim (k/2)^m/\Gamma(m+1)$ and $Y_m(kR) \sim -\frac{1}{\pi}\Gamma(m)(kR/2)^{-m}$ for all integer $m > 0$, and the reflection formulae, and get

$$\hat{s}(m) \to \frac{1}{2|m|} R^{-|m|}, \quad m \in \mathbb{Z} \setminus \{0\}, \quad k \to 0. \tag{13}$$

To analyze convergence rate we will need the asymptotic behavior as $|m| \to \infty$ for fixed k. Using in (12) the large-order asymptotics (9.3.1 in [1]) $J_m(z) \sim \frac{1}{\sqrt{2\pi m}}(ez/2m)^m$ and $Y_m(z) \sim -\sqrt{\frac{2}{\pi m}}(ez/2m)^{-m}$, where z is fixed, gives the leading-order behavior

$$\hat{s}(m) \sim \frac{1}{2|m|} R^{-|m|}, \quad |m| \to \infty, \tag{14}$$

which coincides with the Laplace case (13). We therefore have the exponential uniform bounds, for some constants c_s and C_s depending only on R and k,

$$\frac{c_s}{|m|} R^{-|m|} \leqslant |\hat{s}(m)| \leqslant \frac{C_s}{|m|} R^{-|m|} \leqslant C_s R^{-|m|}, \quad m \in \mathbb{Z} \setminus \{0\}, \tag{15}$$

where C_s is chosen large enough such that $|\hat{s}(0)| \leqslant C_s$ also holds. Fig. 2a shows that for low wavenumber k the leading-order asymptotic is reached rapidly, hence the tightest possible ratio C_s/c_s is not too large (here it is about 10^3). Thus (14) becomes accurate well before the dynamic range begins to exceed machine double precision $\epsilon_{\text{mach}} \approx 10^{-16}$. However, the situation can differ radically for large k, as Fig. 2b illustrates. Here the Laplace asymptotic is not relevant for the eigenvalues within a factor ϵ_{mach} of the maximum. Worse still, the ratio C_s/c_s must be exceedingly large (several tens of orders of magnitude). We will present more useful asymptotic approximations for the eigenvalues in Section 2.4. For now we will use only (15) to prove exponential convergence rates.

2.2. Map from MFS coefficients to Fourier basis

We adapt the above to the discrete source case. Define the density

$$g(\phi) = \sum_{j=1}^{N} \alpha_j \delta(\phi - \phi_j). \tag{16}$$

It follows that

$$u^{(N)}(e^{i\phi}) = \frac{i}{4} \sum_{j=1}^{N} \alpha_j H_0^{(1)}(k|e^{i\phi} - Re^{i\phi_j}|) = (Sg)(\phi).$$

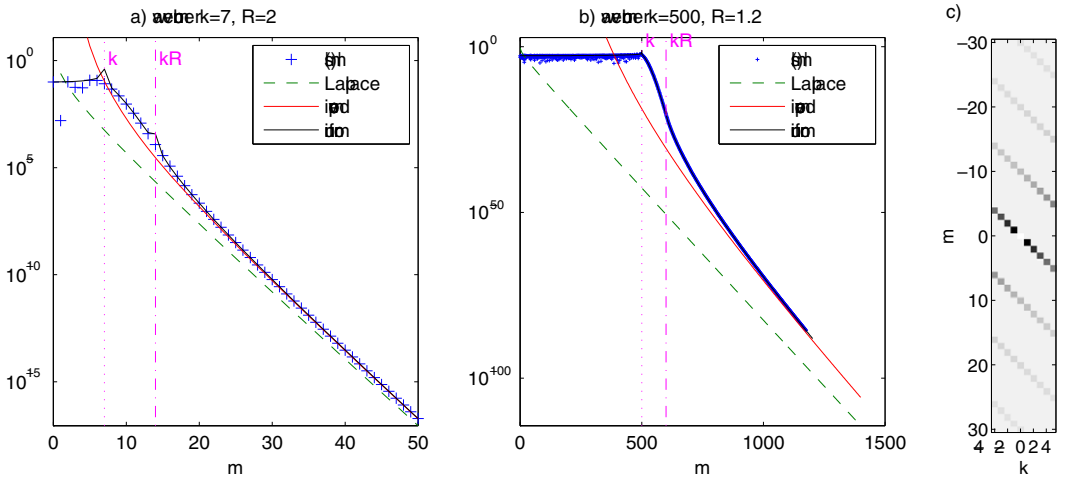

Fig. 2. Comparison for the unit disc of layer potential eigenvalue magnitudes $|\hat{s}(m)|$ given in (12) against various asymptotic expressions: 'Laplace' (14), 'improved' (39), and 'uniform' (40). (a) low wavenumber, (b) high wavenumber. Panel (c) shows density plot of matrix elements (20) of Q for $N = 10$, in the domain $|m| \leqslant 30$. In (c) we chose unrealistically small values of R and k in order to make the super- and sub-diagonals more visible.

We have

$$\|Sg\|^2_{L^2([0,2\pi])} = 2\pi\|\widehat{Sg}\|^2_{\ell^2(\mathbb{Z})} = 2\pi\sum_{m=-\infty}^{\infty}|\hat{s}(m)\hat{g}(m)|^2 = \frac{N^2}{2\pi}\sum_{m=-\infty}^{\infty}|\hat{s}(m)\hat{\alpha}_{m\bmod N}|^2,$$

where $m\bmod N$ denotes the unique integer lying in the range $-N/2+1,\ldots,N/2$ which differs from m by an integer multiple of N. The last equality follows from the Fourier series representation of (16),

$$\hat{g}(m) = \frac{1}{2\pi}\sum_{j=1}^{N}\alpha_j e^{-im\phi_j} = \frac{N}{2\pi}\hat{\alpha}_{m\bmod N}, \quad m\in\mathbb{Z}. \tag{17}$$

Applying Hölder's inequality and (15) we obtain

$$\|Sg\|^2_{L^2([0,2\pi])} \leqslant \frac{N^2}{2\pi}\max_{j=-\frac{N}{2}+1,\cdots,\frac{N}{2}}|\hat{\alpha}_j|^2\cdot\sum_{m=-\infty}^{\infty}|\hat{s}(m)|^2 \leqslant \frac{N^2}{2\pi}|\hat{\boldsymbol{\alpha}}|^2 C_s^2\frac{R^2+1}{R^2-1}. \tag{18}$$

Define the operator $Q:\mathbb{R}^N\to\ell^2(\mathbb{Z})$ by $Q\hat{\boldsymbol{\alpha}} := \widehat{Sg}$, which maps the discrete Fourier coefficient vector $\hat{\boldsymbol{\alpha}}$ to the Fourier series coefficients on the boundary $\partial\Omega$. From (18) we immediately obtain the following.

Lemma 2. *For $R>1$ the operator Q is bounded, with norm*

$$\|Q\| \leqslant C_s\frac{N}{2\pi}\sqrt{\frac{R^2+1}{R^2-1}},$$

where $\|Q\| := \max_{\hat{\boldsymbol{\alpha}}\in\mathbb{R}^N\setminus\{0\}}\frac{\|Q\hat{\boldsymbol{\alpha}}\|_{\ell^2(\mathbb{Z})}}{|\hat{\boldsymbol{\alpha}}|}$.

The action of Q is multiplication by a generalized matrix of width N but (bi-)infinite height,

$$\hat{u}(m) = \sum_{k=-N/2+1}^{N/2} q_{mk}\hat{\alpha}_k, \quad \text{for } m\in\mathbb{Z}. \tag{19}$$

From $Q\hat{\boldsymbol{\alpha}}(m) = (\widehat{Sg})(m) = \hat{s}(m)\hat{g}(m)$ and (17) it follows that the matrix elements are

$$q_{mk} = \frac{N}{2\pi}\hat{s}(m)\delta^{(N)}_{mk}. \tag{20}$$

Fig. 2c shows a greyscale picture of a piece of this matrix. It is dominated by a main diagonal proportional to the diagonal of the S operator defined in (12), but with (exponentially) smaller entries on an infinite sequence of super- and sub-diagonals. This off-diagonal part can be interpreted as aliasing 'overtones' due to discrete sampling of a continuous layer potential. In the Laplace case using (13) in (20) recovers the results of Katsurada [18, Lemma 1, case 2].

2.3. Convergence rate and coefficient sizes in the disc with analytic data

We are now in a position to express the boundary error norm (4) in terms of $\hat{\boldsymbol{\alpha}}$. Combining with (7) and (19) gives

$$t[\hat{\boldsymbol{\alpha}}] = \sqrt{2\pi}\|Q\hat{\boldsymbol{\alpha}} - \hat{\mathbf{v}}\|_{\ell^2(\mathbb{Z})}, \tag{21}$$

where $\hat{\mathbf{v}}\in\ell^2(\mathbb{Z})$ is the vector of Fourier coefficients of the boundary data v on the unit circle. Assume that v can be analytically continued to the annulus $\{z\in\mathbb{C}:\frac{1}{\rho}<|z|<\rho\}$ for some $\rho>1$, that is, the closest singularity of the analytic continuation of v has the radius ρ or $1/\rho$. We then have asymptotically exponential decay of the Fourier coefficients,

$$|\hat{v}(m)| \sim C\rho^{-|m|}, \quad |m|\to\infty \tag{22}$$

for some constant C. A simple example is boundary data arising from an nth-order pole $v(z) = Re(z-\rho)^{-n}$ for $z\in\partial\Omega$, $n=1,2,\ldots$

Minimizing (21) over $\hat{\boldsymbol{\alpha}}$ is a least-squares problem involving the generalized matrix Q. But since the columns of Q are orthogonal this separates into N independent single-variable minimizations. We may use a diagonal approximation to choose $\hat{\boldsymbol{\alpha}}$ which is sufficient for the following convergence rate bounds.

Theorem 3. *Let $R > 1$ and N be even. For analytic boundary data v obeying (22), the minimum boundary error (4) achievable with the MFS in the unit disc satisfies*

$$t \leqslant \begin{cases} C\rho^{-N/2}, & \rho < R^2, \\ C\sqrt{N}R^{-N}, & \rho = R^2, \\ CR^{-N}, & \rho > R^2, \end{cases} \tag{23}$$

where each time C means a different constant which may depend on k, R, and v, but not N. Furthermore if v is analytically continuable to an entire function, the last of the three cases holds for any $R > 1$.

Proof. We choose coefficients $\hat{\alpha}_m = \hat{v}(m)/q_{mm}$ for $-N/2 < m \leqslant N/2$. This exactly matches the Fourier coefficients in this interval, therefore errors are due only to frequencies lying outside the interval. Eqs. (21) & (20) and the triangle inequality in $\ell^2(\mathbb{Z})$ give

$$t = \left(2\pi \sum_{m \notin \left[-\frac{N}{2}+1, \frac{N}{2}\right]} |(Q\hat{\boldsymbol{\alpha}})(m) - \hat{v}(m)|^2 \right)^{1/2} \leqslant \sqrt{2\pi}(E_u + E_v),$$

where

$$E_u^2 = \sum_{m \notin \left[-\frac{N}{2}+1, \frac{N}{2}\right]} |(Q\hat{\boldsymbol{\alpha}})(m)|^2 = \sum_{-\frac{N}{2} < n \leqslant \frac{N}{2}} \left| \frac{\hat{v}(n)}{\hat{s}(n)} \right|^2 \sum_{b \neq 0} |\hat{s}(bN+n)|^2 \tag{24}$$

and

$$E_v^2 = \sum_{m \notin \left[-\frac{N}{2}+1, \frac{N}{2}\right]} |\hat{v}(m)|^2. \tag{25}$$

We can bound both error terms since all terms in the sums have exponential bounds. First we note that using (15) and (22) gives

$$\begin{aligned} E_u^2 &\leqslant C_1 \sum_{\substack{-\frac{N}{2} < n \leqslant \frac{N}{2} \\ n \neq 0}} \left(\frac{R}{\rho}\right)^{2|n|} |n|^2 \sum_{b \neq 0} \frac{R^{-2|bN+n|}}{|bN+n|^2} + C_2 \left| \frac{\hat{v}(0)}{\hat{s}(0)} \right|^2 \sum_{b \neq 0} \frac{R^{-2|bN|}}{|bN|^2} \\ &\leqslant C_1 \sum_{\substack{-\frac{N}{2} < n \leqslant \frac{N}{2} \\ n \neq 0}} \left(\frac{R}{\rho}\right)^{2|n|} \sum_{b \neq 0} R^{-2|bN+n|} + C_2 \left| \frac{\hat{v}(0)}{\hat{s}(0)} \right|^2 \sum_{b \neq 0} R^{-2|bN|} \end{aligned} \tag{26}$$

for sufficiently large constants C_1 and C_2. We can bound

$$\sum_{b \neq 0} R^{-2|bN+n|} \leqslant C_3 R^{-2N+2|n|}, \quad -\frac{N}{2} < n \leqslant \frac{N}{2} \tag{27}$$

for a large enough constant C_3. Inserting (27) into (26) and absorbing $|\frac{\hat{v}(0)}{\hat{s}(0)}|^2$ into the constants gives

$$E_u^2 \leqslant CR^{-2N} \sum_{-\frac{N}{2} < n \leqslant \frac{N}{2}} \left(\frac{R^2}{\rho}\right)^{2|n|} \tag{28}$$

for a sufficiently large constant C. Similarly $E_v^2 \leqslant C\rho^{-N}$ follows from (22). We now study the sum in (28). For $\rho < R^2$, (28) can be estimated by $C\rho^{-N}$ for some constant $C > 0$. This means both E_u^2 and E_v^2 have the same exponential decay $C\rho^{-N}$. For $\rho = R^2$, the sum contains N equal terms and therefore $E_u^2 \leqslant CNR^{-2N}$, which

decays slower than the bound $C\rho^{-N}$ on E_v^2. For $\rho > R^2$, (28) can be estimated by CR^{-2N} for some $C > 0$, which means E_v is of higher negative order in N than E_u and can be dropped. For the case of v continuable to an entire function, we may take $\rho \to \infty$ and the case $\rho > R^2$ applies. □

This is a generalization of a result of Katsurada [15] from the Laplace to the Helmholtz problem. Since only the exponential bounds (15) and no other information about $\hat{s}(m)$ was used, the convergence rates are identical to those for Laplace with the same boundary data.

Remark 4. An interpretation of the two main convergence rate regimes is:

- v is 'not relatively smooth' ($R > \sqrt{\rho}$, i.e. 'distant' charge points): errors are limited by the absence of Fourier modes beyond a frequency $N/2$ in the MFS basis, hence rate is controlled by the boundary data singularity ρ.
- v is 'relatively smooth' ($R < \sqrt{\rho}$, i.e. 'close' charge points): errors are limited by aliasing errors due to the discrete representation of the single layer potential, hence rate is controlled by R.

Remark 5. By keeping track of the constants in the above proof, one can check that C is at least as big as C_s/c_s, which, as discussed, must be very large for large wavenumbers k. Thus although the convergence rates in the theorem are reached asymptotically as $N \to \infty$ in exact arithmetic, we cannot expect the bounds to be numerically useful in practice at large k.

We are interested in how the coefficient norm $|\boldsymbol{\alpha}|$ grows as we reduce the boundary error in the MFS representation (2) by increasing N. Firstly, we now show that when the MFS charge points are closer than the nearest singularity, the coefficients need not grow.

Theorem 6. *Let Ω be the unit disc, and $R < \rho$, with fixed analytic boundary data v obeying (22). Then as $N \to \infty$ there exists a sequence of coefficient vectors $\boldsymbol{\alpha}$ with bounded norm $|\boldsymbol{\alpha}|$, with corresponding boundary error norm (21) converging as in Theorem 3.*

Proof. We choose coefficients as in Proof of Theorem 7, which therefore give the desired convergence rate. Then using (22), (20) and (14),

$$\hat{\alpha}_m = \frac{\hat{v}(m)}{q_{mm}} = \frac{2\pi}{N}\frac{\hat{v}(m)}{\hat{s}(m)} \sim C\frac{|m|}{N}\left(\frac{R}{\rho}\right)^{|m|} \leqslant \frac{C}{2}\left(\frac{R}{\rho}\right)^{|m|}, \quad -\frac{N}{2} < m \leqslant \frac{N}{2}, \quad m \neq 0 \tag{29}$$

for some constant C. For $R < \rho$ this is an exponentially decaying sequence so, independent of N, $|\boldsymbol{\alpha}|$ is bounded by a constant. □

If $\rho < R$, the coefficient choice used in the above two proofs would cause $|\boldsymbol{\alpha}|$ to diverge exponentially with N. It is not immediately obvious whether there is a different choice of $\hat{\alpha}_m$ which avoids such growth. The next result, proved in Appendix A, excludes this possibility by showing that when the singularity in the analytic continuation of the boundary data is closer than the MFS source points, *any* sequence of coefficient vectors $\boldsymbol{\alpha}$ with the desired error norm convergence of Theorem 3 must blow up exponentially.

Theorem 7. *Let Ω be the unit disc, with $R > \rho$. Let the boundary data Fourier coefficients decay no faster than (22), that is, for some constant c_v,*

$$|\hat{v}(m)| \geqslant c_v \rho^{-|m|}. \tag{30}$$

For any positive even N satisfying $N > 3 + N_{\min}$, where $N_{\min} := 2\max\left[\ln\left(\sqrt{\frac{2}{\pi}}\frac{c}{c_v}\right)\Big/\ln\rho, 1\right]$, let $\boldsymbol{\alpha}$ be a coefficient vector such that the MFS representation (2) has a boundary error norm (21) satisfying

$$t \leqslant c\rho^{-N/2}, \tag{31}$$

where c is a constant independent of N. Then

$$|\boldsymbol{\alpha}| \geqslant C\sqrt{N}\left(\frac{R}{\rho}\right)^{N/2} \tag{32}$$

for some constant C which may depend on k, R, and v, but not N.

For MFS approximation in the disc, the immediate consequence is that if ρ is known for given boundary data, to prevent exponential coefficient growth one must restrict the charge point radius to $R \leqslant \rho$. We illustrate this and Theorem 3 with numerical experiments at low wavenumber using the following standard implementation. The integral in (4) is approximated using uniform quadrature with M equally spaced boundary points $\{\mathbf{x}_m\}_{m=1,\ldots,M}$. Specifically we fill a matrix $A \in \mathbb{C}^{M\times N}$ with elements

$$A_{mj} := \frac{i}{4}H_0^{(1)}(k|\mathbf{x}_m - \mathbf{y}_j|), \tag{33}$$

and a boundary value vector $\mathbf{v} \in \mathbb{C}^M$ with elements $v_m := v(\mathbf{x}_m)$, then solve the linear system $A\boldsymbol{\alpha} = \mathbf{v}$. Choosing $M > N$ this is a least-squares problem, and for M sufficiently large the quadrature of the boundary error norm gives $t \approx \sqrt{|\partial\Omega|/M}\,|A\boldsymbol{\alpha} - \mathbf{v}|$. We always choose M large enough that this value of t, and the resulting solution $u^{(N)}$, has converged with respect to M; in practice (on analytic domains) we find this usually requires $M \approx 1.5N$. For the solution of the dense least-squares problem we used the QR decomposition in double precision arithmetic via MATLAB's backslash (`mldivide`) command.

In Fig. 3 we show convergence of t using boundary data

$$v(z) = -\frac{1}{4}Y_0(k|z-\rho|), \quad z \in \partial\Omega \tag{34}$$

with real $\rho > 1$, that is, a single real valued fundamental solution. The three panels illustrate the three cases of Theorem 3. In (a) $\rho > R^2$ thus convergence is determined by R. In (b) $R^2 > \rho > R$ so we have transitioned to a convergence rate given by ρ. In both these cases the coefficient size $|\boldsymbol{\alpha}|$ is very close to constant (note by contrast that the condition number of A, not shown, grows). However in (c) $\rho < R$ so convergence rate is again determined by ρ, but now $|\boldsymbol{\alpha}|$ grows exponentially at precisely the rate indicated by Theorem 7. Fig. 4 shows the resulting approximate field $u^{(N)}$ in the case (c), and the error function $u^{(N)} - u$. Notice that the error is oscillatory at Fourier frequencies of about $N/2$ (as predicted by Remark 4; this can be seen by comparing the alternating signs in Fig. 4b to the angular spacing of source points), is concentrated on the side of $\partial\Omega$ nearest the

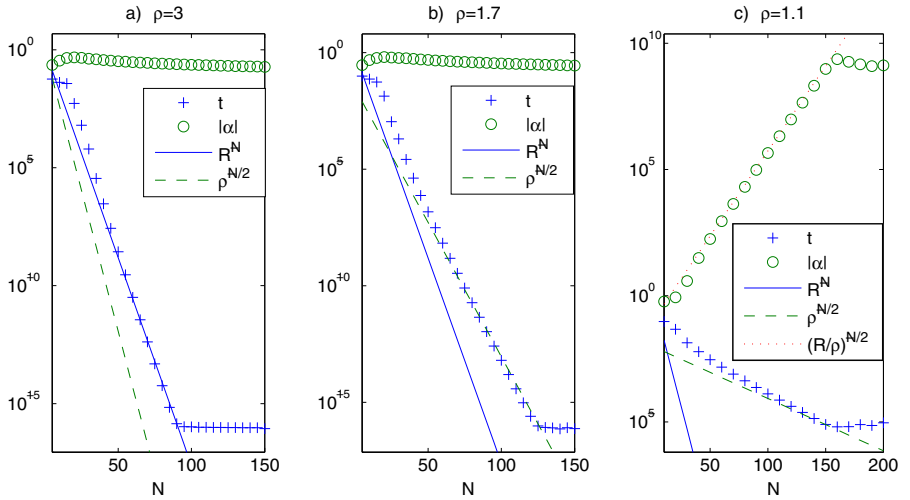

Fig. 3. Convergence and coefficient sizes as a function of N, for the MFS approximation to the interior Helmholtz BVP in the unit disc given boundary data corresponding to a single source (34) at radius ρ. The wavenumber is low ($k = 8$). The MFS sources are at $R = 1.5$. For visual comparison the relevant power laws from Theorems 3 and 7 are shown (sometimes the constants have been chosen to match the data). There were $M = 240$ quadrature points.

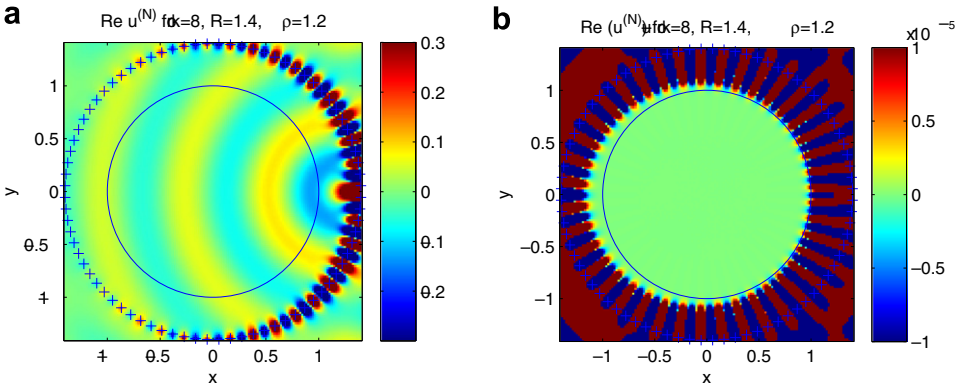

Fig. 4. MFS approximation to the interior Helmholtz BVP in the disc with given boundary data corresponding to a single source (34) outside the domain at $\rho = 1.2$, with $N = 80$ and $R = 1.4$. (a) Re $u^{(N)}$, b) residual error Re $(u^{(N)} - u)$ (note color scale is 3×10^4 times more sensitive than in a).

singularity, and decays exponentially inside the domain (it is evanescent). We have also substituted $v(z) = Re(z - \rho)^{-1}$ and find the convergence rates of Fig. 3 are very similar. We note that in each plot in this figure, the convergence eventually stops, as we now explain.

2.4. Minimum achievable error in the disc for low and high wavenumbers

So far we have proven results which hold in exact arithmetic. However machine precision limits the dynamic range of relevant eigenvalues of S: since the MFS trial functions in (2) have size $O(1)$ in Ω (for any reasonable k), each coefficient α_j will result in round-off errors of size roughly $\epsilon_{\text{mach}}\alpha_j$ in the numerical approximation $u^{(N)}$. Thus we expect convergence to stop when t reaches of order ϵ_{mach} times the coefficient norm $|\boldsymbol{\alpha}|$; this is well illustrated by Fig. 3. In panel (c) the coefficient growth thus limits achievable error norm to only about 10^{-5}. This convergence halting problem has been observed in the Laplace case in the disc [15,19,32] but not analyzed much before. We now analyse this in the Helmholtz case, and first note the following guideline, a consequence of Theorems 3 and 6.

Remark 8. For all k, for boundary data with nearest singularity radius ρ, a choice of charge point radius R in the range $\sqrt{\rho} < R < \rho$ gives optimal asymptotic convergence rate $t \sim \rho^{-N/2}$ and coefficient norm $|\boldsymbol{\alpha}| = \mathrm{O}(1)$.

We now construct a useful heuristic model which predicts, for general ρ and R in the unit disc, both the lowest achievable error norm and the basis size N required to achieve it. We first consider low k, that is, where (14) applies for the relevant eigenvalues (those exceeding $\epsilon_{\text{mach}}\max_m|\hat{s}(m)|$). We discuss both the case $R < \rho$ with $O(1)$ coefficients and the case $R > \rho$ when the coefficient norm grows. Proof of Theorem 7 suggests that, at least when $\hat{s}(m)$ is exponentially decaying, the diagonal approximation for the MFS Fourier coefficients (see (29))

$$\hat{\alpha}_m \approx \frac{2\pi}{N}\frac{\hat{v}(m)}{\hat{s}(m)} \tag{35}$$

approximates the true least-squares Fourier coefficients well, apart from an O(1) number of them lying at extreme frequencies near $m = \pm N/2$. For $R > \rho$ these Fourier coefficients grow exponentially, so dropping an O(1) factor we may consider only the largest coefficient's contribution to the l^2-norm, namely that at $m = N/2$. For $R < \rho$ there is no growth hence the norm is dominated by the coefficients of size O(1) at $m \approx 0$. Combining the two cases, we get the order-of-magnitude estimate at a given N

$$|\boldsymbol{\alpha}| \approx \max\left[\frac{1}{\sqrt{N}}\frac{|\hat{v}(N/2)|}{|\hat{s}(N/2)|}, 1\right]. \tag{36}$$

Similarly, since the boundary data coefficients die exponentially, following Remark 4 and ignoring an $O(1)$ factor we may suppose:

$$t \approx |\hat{v}(N/2)|. \tag{37}$$

We define N_0 to be the N at which convergence stops: for this we use the round-off error consideration $t/|\boldsymbol{\alpha}| \approx \epsilon_{\text{mach}}$ discussed above. In the case $R < \rho$ this implies that convergence halts when t reaches of order ϵ_{mach}, as observed in Fig. 3a and b. However for $R > \rho$, combining (36) and (37) we get an implicit equation for N_0

$$\sqrt{N_0}|\hat{s}(N_0/2)| \approx \epsilon_{\text{mach}} \quad \text{(criterion for halting of convergence, } R > \rho). \tag{38}$$

The minimum achievable boundary error is then given by (37) with the substitution $N = N_0$. As an illustration, using the (Laplace) asymptotic form (14) for the eigenvalues predicts (dropping algebraic factors) that $N_0 \approx 2\ln(1/\epsilon_{\text{mach}})/\ln R$. The parameters of Fig. 3c give $N_0 \approx 180$, then using (22) with $C = 1$ gives $t_0 \approx 10^{-4}$ which, given the heuristic nature of our model, agree well with the observed behavior.

We now briefly discuss the case of high wavenumber. In Fig. 2 we saw that (14) is useless for predicting relevant eigenvalues at high k. We may derive (Appendix B) the asymptotic

$$\hat{s}(m) \sim \frac{1}{2|m|} R^{-|m|} \mathrm{e}^{k^2(R^2-1)/4m}, \quad |m| \to \infty, \tag{39}$$

which Fig. 2a and b shows is improved, but still not useful for the relevant eigenvalues at $k = 500$ (or beyond). Therefore we use the WKBJ method to derive (see Appendix B) a uniform approximation for the eigenvalue magnitudes, defining $a^2 = m^2 - \frac{1}{4}$,

$$|\hat{s}(m)| \approx \begin{cases} [(k^2 - a^2)(k^2R^2 - a^2)]^{-1/4}, & m < k, \\ \frac{1}{2}[(a^2 - k^2)(k^2R^2 - a^2)]^{-1/4} \mathrm{e}^{I_a(k)}, & k < m < kR, \\ \frac{1}{2}[(a^2 - k^2)(a^2 - k^2R^2)]^{-1/4} \mathrm{e}^{I_a(k) - I_a(kR)}, & m > kR, \end{cases} \tag{40}$$

where

$$I_a(x) := \sqrt{a^2 - x^2} - a \ln\left[\left(a + \sqrt{a^2 - x^2}\right)/x\right]. \tag{41}$$

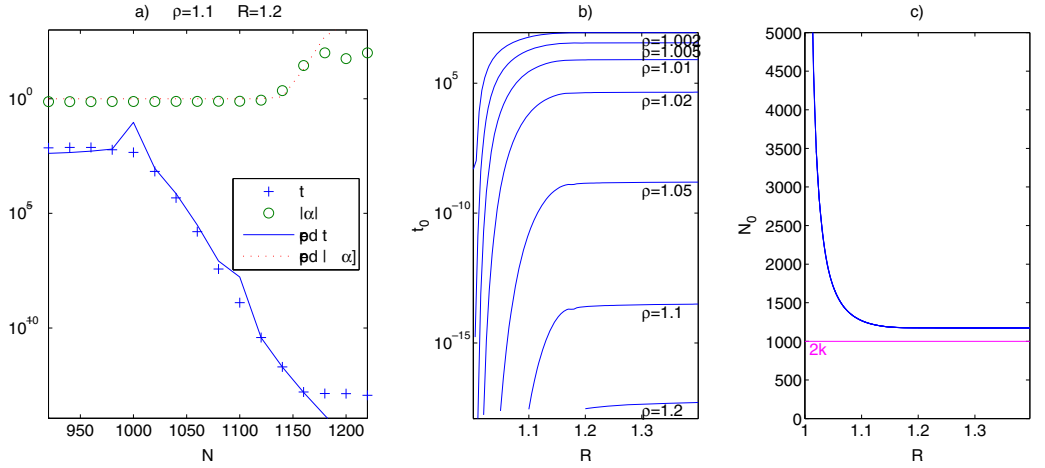

Fig. 5. (a) Convergence and coefficient sizes as a function of N, for MFS approximation of the interior Helmholtz BVP in the disc at high wavenumber $k = 500$, with boundary data (34) with singularity radius $\rho = 1.1$, and MFS sources at $R = 1.2$. The 'predicted' curves are given by (37) using (36), with (40) estimating both $\hat{s}(m)$ and $\hat{v}(m)$. (b) Minimum achievable boundary error norms t_0, and (c) corresponding basis sizes N_0, predicted for a selection of source radii ρ and MFS source point radius R, for $k = 500$, using the model in Section 2.4. Note that in (c) all the graphs for different ρ lie on top of one another.

More precisely this is an estimate of *amplitude* in the oscillatory region ($m < k$) of J_m, and of absolute value in the evanescent region (note $|H_m^{(1)}|$ is never oscillatory). Fig. 2 shows this is a highly accurate asymptotic form in all regions apart from weak algebraic singularities at the two turning points ($J_m(k)$ is at its turning point for $m \approx k$ whereas for $H_m^{(1)}(kR)$ this occurs at $m \approx kR$).

To understand MFS performance at high k in the disc we use the above low-k model (38) with (14) replaced by (40). Fig. 5a shows convergence and coefficient norm at $k = 500$ for boundary data (34), compared with the model predictions. Note that for this boundary data, $\hat{v}(m)$ is given by the right-hand side of (12) with the substitution of ρ for R, which we estimate via (40) with this same substitution. It is clear that, up to the point when convergence halts, the predictions for both error norm and coefficient norm are very close to observations (the largest deviations being spikes due to algebraic singularities discussed above, at $N = 1000$ and 1100).

A crucial feature is that no convergence happens until $N > 2k$, since $\hat{s}(m)$ remains large for $|m| < k$ (see Fig. 2b). One interpretation of this is that $2k$, corresponding to 2 degrees of freedom per wavelength on the perimeter, is the Nyquist sampling frequency for k-bandlimited functions on $\partial\Omega$; in physics this is called the 'semiclassical basis size' [3]. In Fig. 5a, $\rho = 1.1$ so the singularity is $k(\rho - 1)/2\pi \approx 8$ wavelengths from the boundary. In this case convergence is rapid, dropping ten orders of magnitude between $N = 1000$ and $N = 1150$. Convergence then halts, in agreement with (38) which predicts $N_0 \approx 1175$ and $t_0 \approx 3 \times 10^{-14}$ (we find similar agreement for other R and ρ choices). The number of quadrature points was $M = 1500$, or three points per wavelength.

How can R best be chosen to achieve the lowest boundary error for a given high wavenumber k, and ρ? We use the above model to compute N_0 and hence t_0 for a variety of ρ and R at $k = 500$, in Fig. 5b and c. Here the smallest $\rho = 1.002$ corresponds to a singularity only 0.16 wavelengths from the boundary. Two conclusions are clear: (i) If the nearest singularity in the boundary data is at least a few wavelengths away (e.g. $\rho \geqslant 1.1$), then the basis size N need only slightly exceed 2 per wavelength in order to achieve $t_0 \approx \epsilon_{\text{mach}}$. (ii) Fixing ρ, one may achieve $t_0 \approx \epsilon_{\text{mach}}$ as R tends to ρ from above, as expected from Remark 8; however, the basis size required to converge to this error diverges as $\rho \to 1^+$.

3. The MFS on analytic domains

In this section we present results for the MFS on arbitrary analytic domains. On the unit disk we have shown that the MFS coefficients start growing exponentially if the radius R of the charge points becomes larger than the distance ρ of the singularity. The story will be similar for general analytic domains, but with the following twist: singularities may now be due to both boundary data and domain shape. The MFS will be numerically investigated in detail using charge curves defined by exterior conformal maps, which are theoretically important (see Katsurada [17]) and provide a natural generalization of the unit disk case. However, for non-convex domains conformal maps are not always a good choice; we motivate a new method for placing the charge points that instead provides excellent performance. We end with an example where performance exceeds that of BIE. However, to achieve such promising results, an understanding of the singularities is needed, as we now discuss.

3.1. Analytic continuation of solutions

The question of analytic continuation is to find a domain $\tilde{\Omega} \supset \Omega$ and a function $\tilde{u}$ such that $\Delta\tilde{u} + \lambda\tilde{u} = 0$ in $\tilde{\Omega}$ and $\tilde{u}|_\Omega = u$. Since solutions of the Helmholtz equation are real analytic it follows immediately that $\tilde{u}$ is unique.

A classical result of analytic continuation is reflection on a straight arc Γ, on which u satisfies $u|_\Gamma = 0$. Without restriction let Γ be a subset of $\{iy : y \in \mathbb{R}\}$. Then u can be continued across Γ by setting $u(-x, y) := -u(x, y)$ (see also [6]). In [12], Garabedian extended these results to the case that Γ is an arbitrary analytic arc for which $u_\Gamma = 0$. More general reflection principles for linear elliptic PDEs of the type $\Delta u + a(x, y)u_x + b(x, y)u_y + c(x, y) = 0$, where $a(x, y)$, $b(x, y)$ and $c(x, y)$ are real analytic functions were treated by Lewy in [26]. He stated his results for arbitrary Dirichlet, Neumann and mixed boundary conditions but restricted Γ to be a straight line. Representations of the analytic continuation for the case that Γ is not a

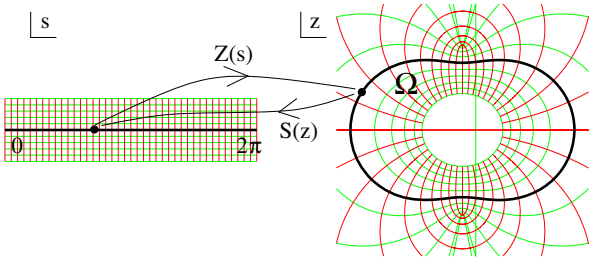

Fig. 6. Illustration of map $Z(s)$ and its inverse $S(z)$ defining a boundary curve $\partial\Omega$. The Schwarz function involves composition of $Z(s)$ and $S(z)$.

straight line were given by Millar in [28]. In [29], he discussed more in detail the analytic continuation of solutions of the Helmholtz equation.

Millar shows that there are two possible sources for singularities of the analytic continuation $\tilde{u}$ of u. The first one comes from singularities of the analytic continuation of the boundary data f. The second possible source of singularities is introduced by the shape of $\partial\Omega$. Let $Z(s) = x(s) + iy(s)$ be a parameterization of $\partial\Omega$, where $s \in [0, 2\pi]$. Assume that $x(s)$ and $y(s)$ are real analytic and that $|Z'(s)| \neq 0$ in $[0, 2\pi]$. Then there exists a complex neighborhood of $[0, 2\pi]$, in which $Z(s)$ is holomorphic and invertible. We denote its inverse by $S(z)$ and define the Schwarz function

$$G(z) := \overline{Z}(S(z)) = \overline{Z(\overline{S(z)})}.$$

Millar showed that except for special cases the singularities of $G(z)$ outside Ω are also singularities of the analytic continuation $\tilde{u}$ of u.

The Schwarz function has been studied in [7]. It is independent of the parameterization of $\partial\Omega$ and has an interpretation in terms of reflection principles on analytic arcs. Assume that z_1 is a point close to $\partial\Omega$. Then its reflection on $\partial\Omega$ can be obtained by the following steps (see Fig. 6):

(1) Compute $t_1 = S(z_1)$.
(2) Reflect t_1 on the real line to obtain the point $t_2 := \overline{t_1}$.
(3) The reflection z_2 of z_1 at $\partial\Omega$ is now obtained as

$$z_2 = Z(t_2) = Z(\overline{t_1}) = Z(\overline{S(z_1)}) = \overline{G(z_1)}. \tag{42}$$

Fig. 7 shows the singularities of the Schwarz function on three different domains, a rounded triangle, an inverted ellipse and a crescent. The domains are defined with default values for the parameters a_1 through a_4, as follows:

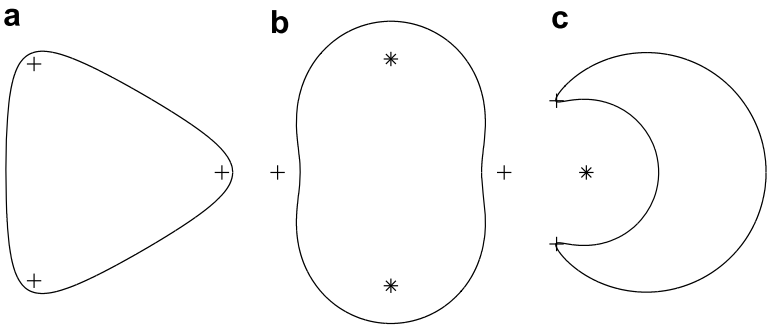

Fig. 7. Domains (left to right): (a) rounded triangle, (b) inverted ellipse, (c) crescent. Branch singularities of the Schwarz function are denoted by + and pole type singularites by ∗. Note in (c) the + signs are inside Ω but very close to the boundary.

$$\text{Rounded triangle}: \quad Z_T(s) = \mathrm{e}^{\mathrm{i}s} + a_1\mathrm{e}^{-2\mathrm{i}s}, \quad a_1 = 0.2$$

$$\text{Inverted ellipse}: \quad Z_{IE}(s) = \frac{\mathrm{e}^{\mathrm{i}s}}{1 + a_2\mathrm{e}^{2\mathrm{i}s}}, \quad a_2 = 0.25$$

$$\text{Crescent}: \quad Z_C(s) = \mathrm{e}^{\mathrm{i}s} - \frac{a_3}{\mathrm{e}^{\mathrm{i}s} + a_4}, \quad a_3 = 0.1, a_4 = 0.9$$

The branch singularities in all three domains are of square root type (see [29] for an analysis of the branch behavior of $G(z)$). The crescent has exterior singularity of pole type at $z = -1/\overline{a_4}$. For the interior Helmholtz problem only the exterior singularities of G are important since these are points where, for generic boundary data, the analytic continuation $\tilde{u}$ of u becomes singular. Conversely if we had an exterior Helmholtz problem then the interior singularities would determine the singularities of the analytic continuation.

3.2. Using exterior conformal map to place the charge points

A natural generalization of the MFS on the unit disk to general analytic domains can be defined in terms of the conformal map from the exterior of the unit disk to the exterior of the domain. This was investigated in the Laplace BVP case by Katsurada [17].

Let Ω be a simply connected domain with analytic boundary $\partial\Omega$. We can parameterize $\partial\Omega$ using the exterior conformal mapping function

$$z = \Psi(w) = cw + c_0 + \frac{c_{-1}}{w} + \frac{c_{-2}}{w^2} + \cdots, \quad c > 0,$$

which maps the exterior $D_1 := \{w : |w| > 1\}$ of the unit disk to the exterior of Ω. The quantity c is called the capacity of Ω. We denote the inverse map by $w = \Phi(z)$. Since $\partial\Omega$ is analytic $\Psi(w)$ can be analytically continued to a domain $D_r := \{w : |w| > r\}$ for some $0 < r < 1$. We denote the conformal radius of a point $z \in \mathbb{C} \setminus \Omega$ by $\rho_z := |\Phi(z)|$.

In the notation of the previous section we may write this parametrization as $Z(s) = \Psi(\mathrm{e}^{\mathrm{i}s})$ since the unit disc is parametrized by $w = \mathrm{e}^{\mathrm{i}s}$. Using that the reflection of a point z on the unit circle is given by $z' = \frac{1}{\bar{z}}$ the Schwarz function may now be written $G(z) = \overline{\Psi(1/\overline{\Phi(z)})}$; it follows that it is analytic in $\{z \in \mathbb{C} : 1 < \rho_z < \frac{1}{r}\}$.

In the unit disk case we placed the MFS points equally distributed on a curve with radius R. For general analytic domains we now place the points on a curve $\Gamma_R := \{z : \rho_z = R\}$ with constant conformal radius $\rho_z = R$. On this curve we distribute the points equally spaced in conformal angle, that is

$$\mathbf{y}_j := \Psi(\mathrm{e}^{2\pi\mathrm{i}j/N}), \quad j = 1, \ldots, N. \tag{43}$$

If Ω is the unit disk this definition coincides with that of Section 2. Replacing the disk radii R and ρ in Theorem 3 by the corresponding conformal radii we obtain the following conjecture for the rate of convergence of the MFS for Helmholtz problems on general analytic domains.

Conjecture 9. *Let t be the error of the MFS as defined in (4) by placing the MFS points equally distributed in conformal angle at a conformal distance R around Ω. Let $\rho > 1$ be the conformal radius of the closest (in the sense of conformal radius) singularity of the analytic continuation of u. Then*

$$t \leqslant \begin{cases} C\rho^{-N/2}, & \rho < R^2, \\ CR^{-N}, & \rho > R^2, \end{cases} \tag{44}$$

where C is a constant that may depend on Ω, k, R and v, but not N. Furthermore, if u continues to an entire function, the latter case holds for any $R > 1$.

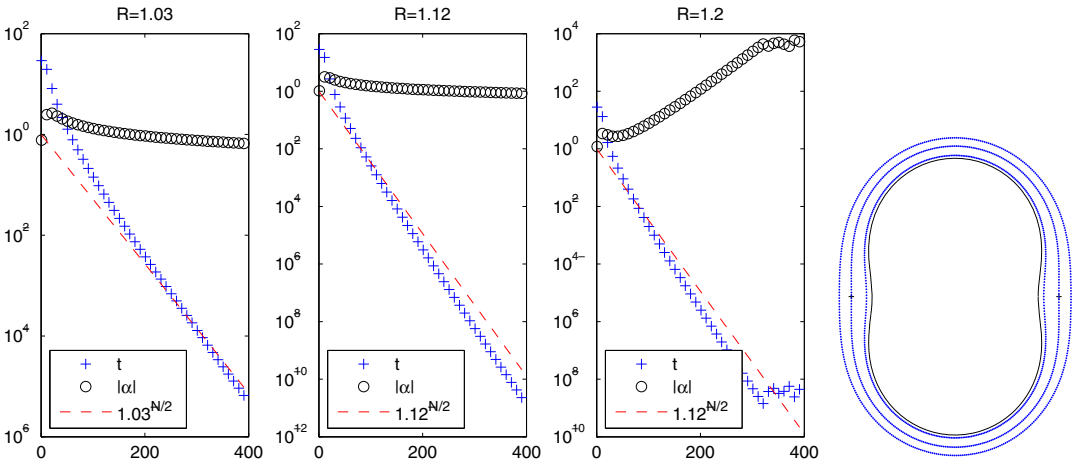

Fig. 8. Left three plots: Estimated (dashed lines) and observed ('+') rates of convergence of the MFS on the inverted ellipse for charge points with conformal radii $R = 1.03$, $R = 1.12$ and $R = 1.2$. The corresponding coefficient norms $|\boldsymbol{\alpha}|$ are denoted by 'o'. Right plot: Domain and positions of the charge points (shown as dots) for the above three conformal radii, with branch-type singularity locations (+ signs).

Remark 10. The first case ($\rho < R^2$) of this conjecture was proved in the Laplace case by Katsurada in [17] under additional restrictions on the analytic continuation of Ψ into the unit disk. In numerical studies we have observed that these conditions are not necessary to achieve the given convergence rates, so do not include them in our conjecture (compare also Remark 3.2 of [17]). We do not state a conjecture for the case $\rho = R^2$ since numerically it cannot be established if for general domains the same algebraic factor is needed as for the disk.

In Fig. 8 we plot the observed error t for the MFS on the inverted ellipse of Fig. 7, for wavenumber $k = 5$ and constant boundary condition $v \equiv 1$. The estimated rates from Conjecture 9 are denoted by dashed lines. The three plots correspond to MFS points placed at the conformal distances $R = 1.03$, $R = 1.12$ and $R = 1.2$. The conformal radius $R = 1.12$ is also the approximate conformal radius ρ of the two singularities. The corresponding MFS curves are shown on the right of Fig. 8. The estimated convergence rates are in all three cases in good agreement with the observed error t.

In the disk case we can observe exponential coefficient growth once the radius R of the charge points is larger than the radius ρ of the singularity of the analytic continuation of u (see Theorem 7). For general analytic domains we observe a similar behavior. To demonstrate this we plotted in Fig. 8 also the norm $|\boldsymbol{\alpha}|$ of the MFS coefficients. As long as the conformal radius R of the MFS points is smaller or equal to the conformal radius ρ of the singularities we do not observe any growth of $|\boldsymbol{\alpha}|$ for growing N (first two plots of Fig. 8). In the third plot we have $R > \rho$ and $|\boldsymbol{\alpha}|$ grows exponentially for growing N. It is instructive to compare this figure panel by panel against Fig. 3.

This leads to the following conjecture, which mirrors Theorems 6 and 7.

Conjecture 11. *Let Γ be any Jordan curve enclosing $\overline{\Omega}$, with $\operatorname{dist}(\Gamma, \partial\Omega) > 0$, on which MFS charge points are chosen asymptotically densely. Then the coefficient norm $|\boldsymbol{\alpha}|$ that minimizes t grows asymptotically exponentially as $N \to \infty$ if and only if Γ encloses a singularity of the analytic continuation of u.*

We stated this conjecture for general Jordan curves, since numerical experiments suggest that there is only coefficient growth if the curve encloses a singularity of the analytic continuation. This conjecture is analogous to (but stronger than) a result that coefficients grow if all singularities are *not* enclosed by Γ in the context of exterior scattering [8, Chapter 4, Theorem 2.4].

In Fig. 9 we show the coefficient norm $|\boldsymbol{\alpha}|$ and the approximation error t for a growing conformal distance R of the MFS source points and fixed number N in four different cases: the unit disk and the three domains from Fig. 7. In all cases we have used $k = 5$. For the disk the boundary data is given by (34) with singularity location $\rho = 1.2$, and in the other three cases by $v(z) \equiv 1$ (recall that here the Schwarz function introduces singularities in u). The

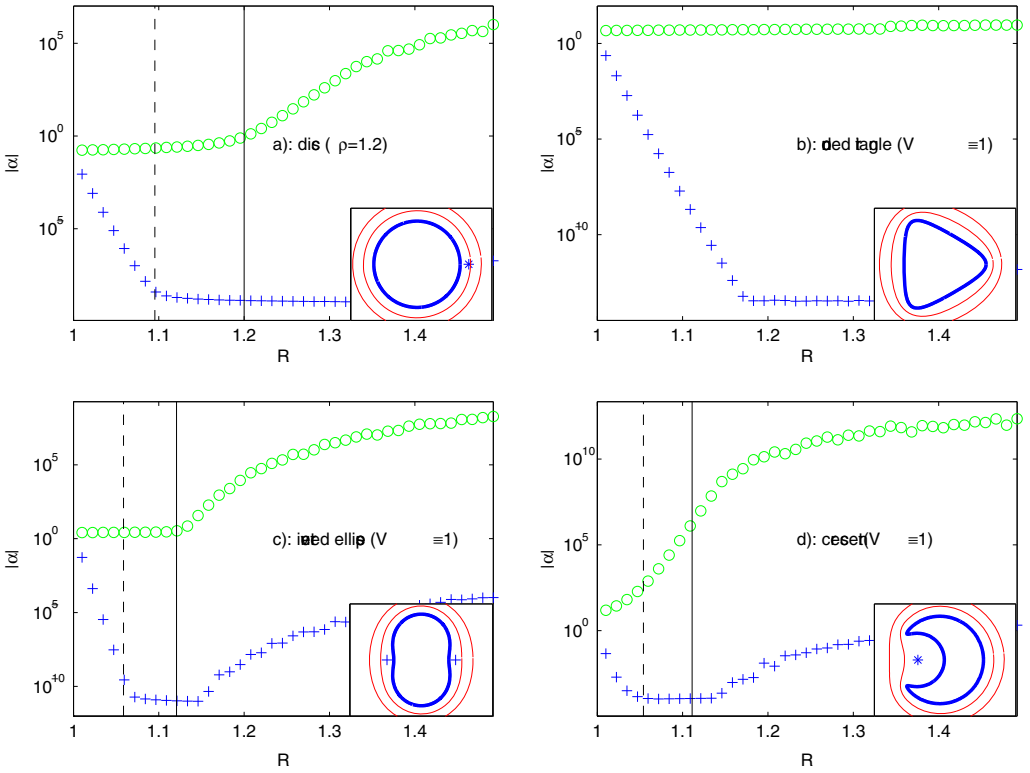

Fig. 9. Growth of coefficient norm $|\boldsymbol{\alpha}|$ (circles), and least-squares approximation error t ('+' signs), for (a) the unit disc with boundary data (34), and (b–d) the three other shapes of Fig. 7 with constant boundary data $v \equiv 1$. MFS points are chosen on curves with constant conformal radius R. The insets show domains, exterior singularities using same notation as Fig. 7, and curves with conformal radius $R = 1.24$ and 1.49. The parameters are $k = 5$. $N = 200$ for a and b, $N = 400$ for c and d. The number of quadrature points M on $\partial\Omega$ is chosen sufficiently large throughout.

vertical solid lines denote the conformal radius ρ of the singularities of the analytic continuation of u and the vertical dashed lines denote the square root $\rho^{1/2}$. Since the Schwarz function for the rounded triangle does not have any singularities in the exterior of the domain the solution u can be analytically continued to an entire function.

For the disk, the inverted ellipse and the crescent the error t does not decrease further once R passes the dashed line. This can be expected from Conjecture 9 since the upper bound on the error t does not decrease any more for fixed N and $R > \rho^{1/2}$.

For these three domains we can also observe exponential coefficient growth of $|\boldsymbol{\alpha}|$ for fixed N when $R > \rho$. For the crescent this exponential growth already starts earlier. However, this is not a contradiction to Conjecture 11. The conjecture treats the case of a fixed curve and $N \to \infty$. This does not exclude the existence of transient growth effects if the singularity lies outside the curve containing the charge points.

An explanation for these transient effects in the crescent case is that close to the pole-like singularity of the Schwarz function we need a very high number N of basis functions to sufficiently resolve a highly oscillatory Helmholtz field.

Another interesting special case is the rounded triangle. Since the analytic continuation of u is an entire function, by Conjecture 11 we do not expect any exponential growth of $|\boldsymbol{\alpha}|$. Indeed, Fig. 9b shows that $|\boldsymbol{\alpha}|$ stays virtually constant as R increases.

3.3. Using a singularity-adapted curve to place the charge points

The above exterior conformal method has the following problem: in any concave parts of Ω the exterior conformal map Ψ has a very (in fact, exponentially) large gradient. This well-known property of conformal maps is related to the so-called crowding problem. This has two consequences for concave regions: the spacing

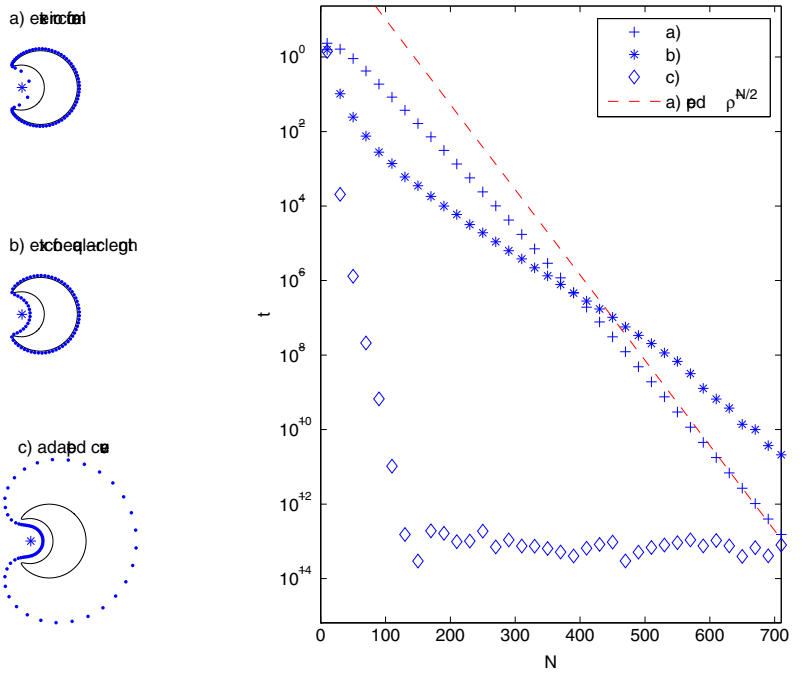

Fig. 10. Convergence rate for the crescent domain (with $a_3 = 0.1, a_4 = 0.9$) illustrating the concavity problem. The wavenumber is $k = 3$ and constant boundary data $v \equiv 1$. For (a) and (b) MFS charge points are placed on an exterior conformal curve at $R = \sqrt{\rho}$ where $\rho = 1/a_4$ is the singularity conformal distance. The point spacing is equal in (a) conformal angle, and (b) arc-length. (c) Adapted curve and spacing given by (45), see Section 3.3. The dashed line shows the predicted convergence rate for (a), a_4^N.

of charge points according to (43) becomes very large, and as R is increased from 1, the curve Γ_R moves away from $\partial\Omega$ very rapidly. Both these effects are illustrated by the MFS charge curve for the crescent in Fig. 10a.

This means that Schwarz function singularities which are a moderate distance from a concave part of $\partial\Omega$ may actually have a conformal radius extremely close to 1. The net result is that if the coefficient growth of Conjecture 11 is to be prevented, R must be very close to 1, hence by Conjecture 9 the convergence rate is necessarily very poor. For example, in Fig. 10, the conformal radius of the pole in the Schwarz function is only $\rho = 1/a_4 \approx 1.11$, and the observed rate for case a) approaches the predicted $\rho^{-N/2}$ (dashed line in the figure). One can attempt to fix the problem of the large point spacing by retaining the same MFS curve Γ_R but choosing charge points equally spaced in arc-length, as illustrated in Fig. 10b. Despite an initial improvement for small N, the asymptotic convergence rate turns out to be no better than in case a), and is believed to be the same (for errors $t < 10^{-6}$ it performs worse, we believe due to a lack of point density near the 'spiked' parts of the crescent).

In Fig. 10c we show a different 'adaptive' choice of MFS curve and point spacing which clusters charge points near the singularity but spreads them out (while taking them further away from $\partial\Omega$) away from the singularity. This gives a convergence rate over five times faster than the exterior conformal curve, for instance an error of $t \approx 10^{-13}$ is reached for $N = 140$ as opposed to $N = 730$ for case a). This simple adaptive method is based on the idea of replacing the exterior conformal map by an annular one, as follows.

From the discussion in Section 3.1, the map $Z(s)$ defines an annular conformal map which is one-to-one for s in some strip around $[0, 2\pi]$, as in Fig. 6. The external singularities control convergence rate; we label them by $\sigma = 1, \ldots, P$, where P is the number of singularities. They have s-plane locations $s_\sigma = \chi_\sigma - \mathrm{i}\tau_\sigma$ with $\tau_\sigma > 0$, Their minimum distance to the real axis is $\tau := \min_\sigma \tau_\sigma$. Katsurada et al. [19] have discussed using such an annular map to place charge points for the Laplace BVP, according to $\mathbf{y}_j := Z(2\pi j/N - \mathrm{i}\log R)$ for some $R > 1$; note this is the annular map equivalent of (43). A related annular map method has been tried in the scattering case [14]. According to Conjecture 11 in order to prevent coefficient growth in this case one would need to choose $\log R < \tau$. This may be a severe restriction: for example one may check that the crescent formula $Z_C(s)$ in Table 3.1 is identical to this domain's exterior conformal map Ψ, thus the concavity effect causes τ to be very small.

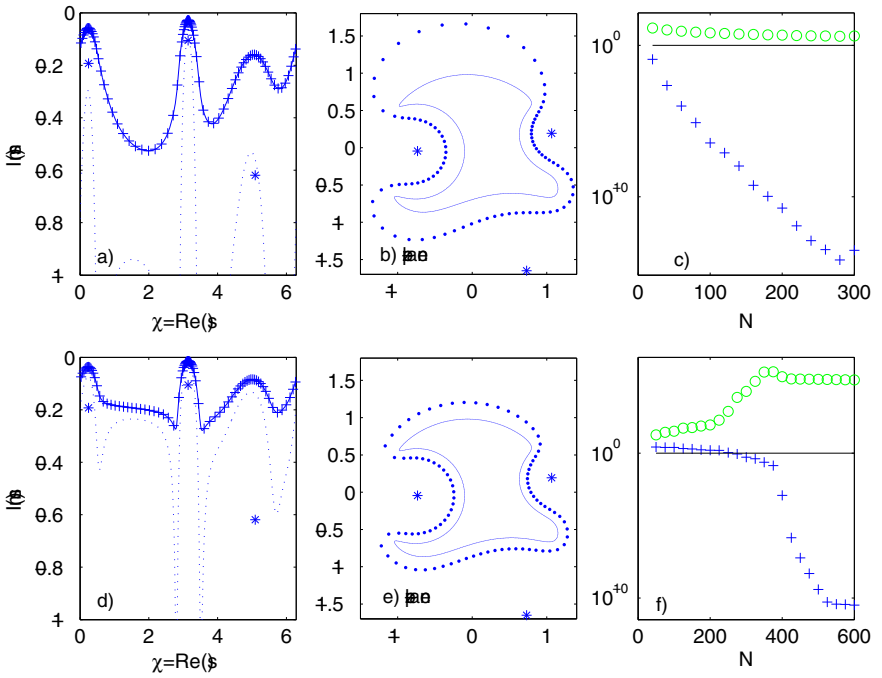

Fig. 11. Generalized crescent analytic domain parametrized by (47), showing performance of adaptive charge points of Section 3.3. The top row is at $k = 3$, the bottom row at $k = 100$. (a) and (d) show the curve $y(\chi)$ and the locations $(\chi_j, y(\chi_j))$ in the s-plane, the singularities s_σ ('$*$' symbols), and the distance-limiting function $|Z\prime(\chi)|/D_{\max}$ (dotted line). (b) and (e) show the charge locations (for clarity, $N = 90$ has been used in both cases). (c) and (f) shows error norm convergence t ('+' symbols) and coefficient norm $|\boldsymbol{\alpha}|$ ('o' symbols).

However, there are an infinite family of annular maps $Z(s)$ which parametrize the *same* boundary $\partial\Omega$, and these may have differing Schwarz singularity locations in the s-plane. Given an analytic domain Ω one is free to choose between such parametrizations. Ideally, our goal is to choose one with as large a τ as possible, to achieve a high convergence rate. However, we find it convenient to retain the given parametrization $Z(s)$, and instead build a charge curve in the s-plane which no longer has constant imaginary part, and which captures the spirit of such a reparametrization. Our curve is given by $s = \chi - \mathrm{i}y(\chi)$, where $\chi \in [0, 2\pi]$ is the real part of s, and the function y is given by

$$[y(\chi)]^{-1} = \left(\frac{D_{\max}}{|Z'(\chi)|}\right)^{-1} + \sum_{\sigma=1}^{P} \left[\gamma\tau_\sigma + \beta\frac{1-\cos(\chi-\chi_\sigma)}{\tau_\sigma}\right]^{-1}, \tag{45}$$

where parameter values performing well in most domains are $\beta = 0.7$ (interpreted as a curvature factor), $\gamma = 0.4$ (expressing the curve's fractional distance to each singularity), and

$$D_{\max} = \max[1, 25/k] \tag{46}$$

is interpreted as the maximum allowable distance of the curve from $\partial\Omega$. Eq. (45) has the effect of bringing the curve close to $\partial\Omega$ in the vicinity of each singularity (via each cos term in the sum) in the style of an equipotential curve, while allowing it to move up to $D_{\max}$ from the boundary in the absence of nearby singularities. Given the curve function $y(\chi)$ a set of N real values $\{\chi_j\} \in [0, 2\pi]$ are then chosen such that their local spacing is proportional to $y(\chi)$.[1] The MFS charge points are then given by $\mathbf{y}_j = Z(\chi_j - iy(\chi_j))$.

In Fig. 11, we illustrate the performance of this method on a generalization of the crescent domain given by

[1] In practice this can easily be done numerically by solving the ODE $g'(\chi) = 1/y(\chi)$ then spline fitting to construct an approximate inverse function g^{-1}.

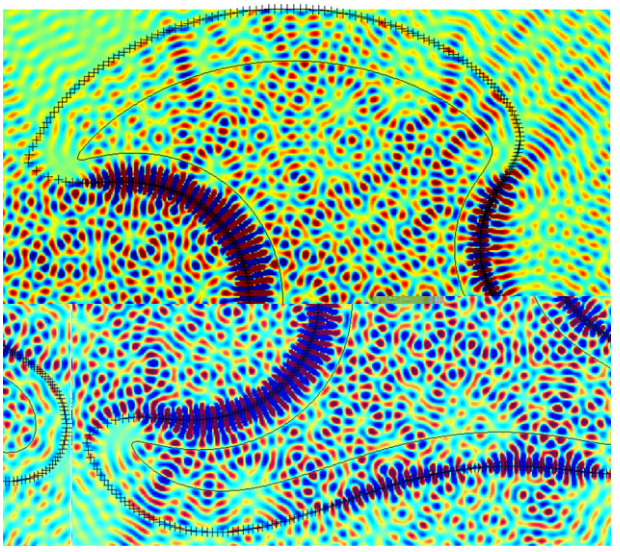

Fig. 12. Interior Helmholtz BVP solution u for the same domain as Fig. 11, at $k = 100$, with boundary data $v \equiv 1$, using as basis size of $N = 525$, and $M = 1000$ boundary points. Error norm is $t = 5 \times 10^{-11}$. The boundary (thin solid line) and charge points ('+' symbols) are shown, and the field u from (2) is shown both outside and inside Ω. CPU time was 2.9 s to compute the coefficient vector $\boldsymbol{\alpha}$, and 5.4 min to evaluate the solution u shown (2.4×10^5 points on a grid of spacing 0.005).

$$\text{Generalized crescent}: \quad Z_{GC}(s) = \mathrm{e}^{\mathrm{i}s} - \frac{0.1}{\mathrm{e}^{\mathrm{i}s} + a_5} - \frac{0.07 + 0.02\mathrm{i}}{\mathrm{e}^{\mathrm{i}s} + a_6} + \frac{0.2}{\mathrm{e}^{\mathrm{i}s} + a_7} \tag{47}$$

with $a_5 = 0.9$, $a_6 = -0.8 - 0.2\mathrm{i}$, $a_7 = -0.2 + 0.5\mathrm{i}$. The Schwarz function has three exterior pole type singularities, shown by * symbols, with s-plane locations $1/\overline{a_5}$, $1/\overline{a_6}$, and $1/\overline{a_7}$. The two rows of subfigures contrast the effect of $D_{\max}$ given by (46) at low vs high wavenumbers. For low wavenumber $D_{\max}$ is large and the contribution of the first term in (45) is small. This enables the curve to reach large negative Im s, hence large distances from $\partial\Omega$ and a large point spacing, in regions away from singularities. We observe rapid convergence, reaching $t = 10^{-14}$ by $N = 280$, and no exponential coefficient growth. As k increases, $D_{\max}$ drops and the first term in (45) starts to become significant (see dotted line in Fig. 11d), and has the effect of bringing the curve closer to the domain. As $k \to \infty$ this term dominates and the curve tends to a constant distance of about 4 wavelengths from $\partial\Omega$ everywhere on the curve. The bottom row in the figure shows the case $k = 100$. Once $N = 400$ (about 3.0 degrees of freedom per wavelength on the boundary), convergence is rapid, reaching 10^{-10} at $N = 525$. Since the coefficient norm $|\boldsymbol{\alpha}| \approx 10^5$ convergence halts here. The resulting solution u is shown in Fig. 12.[2] Values outside Ω have been included to highlight the manner in which the MFS points generate the field (very large coefficients are easily noticed due to the dark, highly oscillatory bands in these parts of Γ).

3.4. Performance of singularity-adapted MFS at high wavenumber

Finally, we test the performance of the above method for different shape at higher wavenumber, as shown in Fig. 13. This domain is challenging since it has, very close to the boundary, five exterior branch-type singularities in the Schwarz function. We also choose nonconstant boundary data which itself has a singularity (however since it is outside Γ there is no need to include its contribution in the curve formula (45)). There are about 165 wavelengths across the domain's maximum diameter. Boundary error t of order 10^{-10} is reached using $N = 1900$ corresponding to 3.3 basis functions per wavelength on the perimeter. Since $|\boldsymbol{\alpha}| \approx 10^4$, this

[2] Computation times are quoted for a single core of a 2 GHz Intel Core Duo laptop CPU, with 2 GB RAM, running GNU/Linux, coded in MATLAB. For evaluation of u the sum (2) was performed naively. The MATLAB Hankel function routine is also by no means optimal, requiring on average 2.3 μs per evaluation.

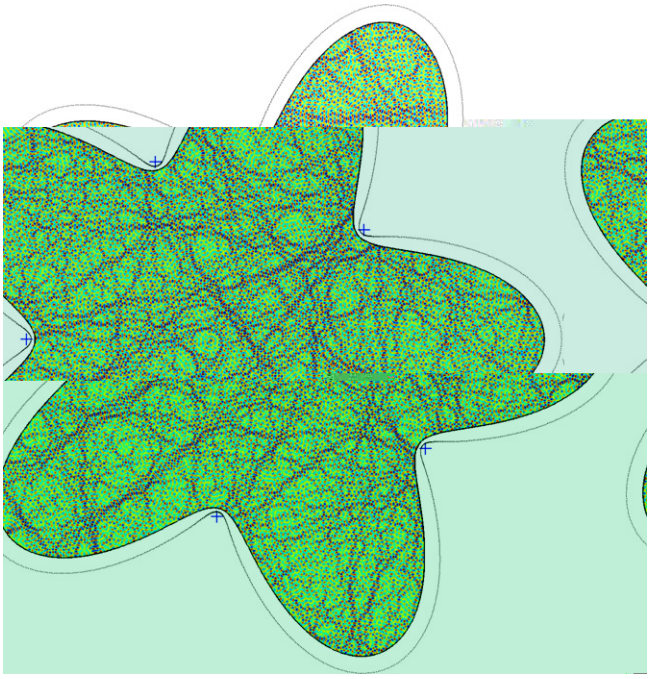

Fig. 13. Interior Helmholtz BVP solution u for the analytic star domain defined by radial function $r(\theta) = 1 + 0.3\cos(5\theta)$ at wavenumber $k = 400$, boundary data $v(z) = \mathrm{Re}\,(z-\rho)^{-1}$ and $\rho = 1 + 0.5\mathrm{i}$. The color scale shows a u range $[-45, 45]$. Boundary error norm is $t = 3.6 \times 10^{-10}$, and interior values agree to 10^{-11} relative error against a BIE computation. Basis size was $N = 1900$ and $M = 2800$ quadrature points. Charge points are shown by dots and Schwarz branch singularities by + symbols. CPU time was 55 s to compute the coefficient vector $\boldsymbol{\alpha}$, and 1.0 h to evaluate the interior solution u shown (8.2×10^5 points on a grid of spacing 0.002).

value of t cannot be decreased much by increasing N. At fixed N, an adequate number M of quadrature points was found by increasing until interior values of the solution converged (seemingly spectrally) to the required number of digits.

We have verified that a pointwise error of order 10^{-12} times typical u values is achieved in the interior, by comparison against a BIE solution implemented with Martensen–Kussmaul spectral quadrature of the double layer potential, as recommended in [5, Section 3.5]. For instance, with the above parameters the MFS value of $u^{(N)}(0.045 + 0.1\mathrm{i})$ is $-50.189873472429 - 1.5 \times 10^{-11}\mathrm{i}$ compared to for BIE $-50.189873472414 + 5 \times 10^{-12}\mathrm{i}$. Note that the exact solution is real, and resonance makes its size roughly 10^2 times the O(1) boundary data. This MFS error is much better than the bound (5), which gives relative error of order 10^{-7} since d (defined below (5)) is very small, of order 10^{-5}. We note that to achieve the above the BIE required a larger linear system, $N = 3200$ Nyström quadrature points (these were equally spaced in θ which may not be optimal), and required 91 s of CPU time to compute the layer density coefficients, as opposed to 55 s for MFS. This serves to illustrate the potential MFS has for high frequency problems.

In domains with more distant singularities, we find barely more than 2 basis functions per wavelength are sufficient in the high k limit, similar to what was found for the disc in Section 2.4. We postpone further study of important issues such as choice of $D_{\max}$ at high wavenumber, and more detailed comparison with BIE, to future work.

4. Conclusions

The Method of Fundamental Solutions is a powerful tool for solving the Helmholtz BVP, but, as we have demonstrated, the achievable accuracy is limited by the size of the coefficient norm $|\boldsymbol{\alpha}|$ (as opposed to the condition number). Therefore we have analysed, for the first time, the growth of $|\boldsymbol{\alpha}|$ with basis size N as one converges towards Helmholtz solutions in the disc and other analytic domains. In the disc we have theorems on

convergence rate (Theorem 3) and coefficient growth (Theorems 6 and 7), and for analytic domains we have corresponding conjectures (Conjectures 9 and 11) supported by numerical experiments in many domain shapes. These show that the success (numerical stability and hence high accuracy) of the MFS relies on a choice of charge curve which does not enclose any singularities of the analytic continuation of the solution u. These singularities are associated either with the analytic continuation of the boundary data, or with the Schwarz function of the domain.

The conclusions for optimal choice of MFS charge points are as follows. For the unit disc, with concentric equally spaced charge points, a radius between $\sqrt{\rho}$ and ρ is optimal (Remark 8), ρ being the radius of the nearest singularity in boundary data. For general analytic domains, charge points placed on a curve which adapts to the singularity locations have been shown to perform very well. At high wavenumber we show that in the disc asymptotically two basis functions per wavelength on the boundary are needed, and that in more complicated nonconvex domains with nearby singularities this need only increase by less than a factor of two to achieve error norms close to machine precision. In practice this unusually small N results in rapid solution of the basis coefficients using dense linear algebra, even at high wavenumber.

Although the goal of this work is not a detailed comparison of MFS against boundary integral equations (BIE), our experiments show that MFS can be highly competitive, with a smaller basis size N, and the advantage that accurate solutions are easy to evaluate up to the boundary. MFS is useful only if condition number is not a problem, which is true for direct solvers but not iterative ones. Thus we do not expect MFS can benefit in the way BIE do from Fast Multipole (FMM) acceleration in an iterative solver. However, recent developments in fast direct solvers [27] could remove this problem and allow MFS to be efficient in large-scale ($N > 5000$) settings.

As with BIE, the CPU time to evaluate the interior solution at several grid points per wavelength is much larger than the coefficient solution time, especially using a naive implementation of the sum (2) and MATLAB's Hankel function routine. Replacing this evaluation of u with a FMM summation would be a natural next step and is expected to result in a large speedup at high wavenumbers.

We expect our findings on coefficient growth rates, and the new adaptive charge curve algorithm, to be easily extendable to the exterior Helmholtz scattering problem, for which MFS has shown promise in the engineering community [24,14,8].

Acknowledgments

AHB is supported by the National Science Foundation under Grant DMS-0507614. TB is supported by Engineering and Physical Sciences Research Council Grant EP/D079403/1. TB wishes to thank the DMV, the DFG, and the Shapiro Visitor Program, for a joint travel grant in January 2007 to visit Dartmouth. This work benefitted from important discussions with Lehel Banjai, Leslie Greengard, David Karkashadze, Fridon Shubitidze, and Nick Trefethen, and from the reviewer comments.

Appendix A

Proof of Theorem 7 For even N fix $N > N_{\min} + 3$. Using (20) in (21) implies the trivial bound

$$\sqrt{2\pi}\left|\frac{N}{2\pi}\hat{s}(m)\hat{\alpha}_{m \bmod N} - \hat{v}(m)\right| \leqslant t \quad \text{for all } m \in \mathbb{Z}. \tag{A.1}$$

Define the (positive) maximum Fourier frequency $F := \frac{N}{2} - K$, where K is the unique integer such that

$$\frac{N_{\min}}{2} \leqslant K < \frac{N_{\min}}{2} + 1.$$

Note that K is independent of N. One can verify using (31), (30) and the definition of $N_{\min}$ that

$$|\hat{v}(m)| \geqslant \sqrt{\frac{2}{\pi}}\, t \quad \text{for all } |m| \leqslant F. \tag{A.2}$$

In the frequency range $|m| \leqslant F$, it follows from (A.1) and (A.2) that $\hat{v}(m)$ is sufficiently large relative to t to bound the coefficients away from zero,

$$|\hat{\alpha}_m| \geqslant \frac{2\pi}{N}\frac{|\hat{v}(m)| - t/\sqrt{2\pi}}{|\hat{s}(m)|} \geqslant \frac{\pi}{N}\frac{|\hat{v}(m)|}{|\hat{s}(m)|} \geqslant \frac{\pi c_v |m|}{C_s N}\left(\frac{R}{\rho}\right)^{|m|}, \quad 0 < |m| \leqslant F, \tag{A.3}$$

where the last step used (15) and (30). Choosing the maximal frequency $m = F = \frac{N}{2} - K$ we obtain

$$|\hat{\alpha}_F| \geqslant \frac{\pi c_v}{C_s}\left(\frac{R}{\rho}\right)^{\frac{N}{2}-K}\left(\frac{1}{2} - \frac{K}{N}\right) > \frac{\pi c_v}{2C_s}\left(\frac{R}{\rho}\right)^{\frac{N}{2}-K}\frac{1}{N_{\min}+3}. \tag{A.4}$$

Here the latter inequality follows from

$$\frac{1}{2} - \frac{K}{N} > \frac{1}{2} - \frac{N_{\min}/2+1}{N_{\min}+3} = \frac{1}{2(N_{\min}+3)}.$$

Absorbing the N-independent factors of (A.4) into a constant and noticing that the Euclidean norm of a vector is at least as large as its largest component we have

$$|\boldsymbol{\alpha}| = \sqrt{N}|\hat{\boldsymbol{\alpha}}| \geqslant \sqrt{N}|\hat{\alpha}_F| \geqslant C\sqrt{N}\left(\frac{R}{\rho}\right)^{N/2} \tag{A.5}$$

for a sufficiently small constant $C > 0$, as claimed in the theorem. □

Appendix B. Bessel function asymptotics

We take the standard Taylor series [1]

$$J_m(z) = \left(\frac{z}{2}\right)^m \sum_{k=0}^{\infty} \frac{(-z^2/4)^k}{k!(m+k)!} \tag{B.1}$$

and in the large-m limit we may approximate $(m+k) \approx mm^k$, then recognize the power series for the exponential, giving

$$J_m(z) \sim \frac{1}{m!}\left(\frac{z}{2}\right)^m \mathrm{e}^{-z^2/4m}, \quad m \to \infty. \tag{B.2}$$

Similarly the standard series

$$Y_m(z) = -\frac{1}{\pi}\left(\frac{z}{2}\right)^{-m} \sum_{k=0}^{m-1} \frac{(m-k-1)!(z^2/4)^k}{k!} + \frac{2}{\pi}\ln(z/2)J_m(z) + O(z^m) \tag{B.3}$$

with $(m-k-1)! \approx m!/m^k$ gives

$$Y_m(z) \sim -\frac{m!}{\pi}\left(\frac{z}{2}\right)^{-m} \mathrm{e}^{z^2/4m}, \quad m \to \infty. \tag{B.4}$$

Neither of these asymptotic forms are given in [1], however (B.2) has been recently noted in the physics community [25]. Combining these two in (12), using the reflection formulae, and ignoring the lower-order J contribution to the Hankel function, gives (39).

Bessel's equation $u'' + u'/r + (1 - m^2/r^2)u = 0$ with the Liouville transformation $w = r^{1/2}u$ then changing variable to $x = r/a$, with $a^2 = m^2 - \frac{1}{4}$, gives the ODE

$$\frac{d^2w}{dx^2} + a^2\left(1 - \frac{1}{x^2}\right)w = 0. \tag{B.5}$$

The WKBJ (or Liouville–Green) asymptotic approximation (Chapter 9.3 of [30]) for large parameter a is then

$$w(x) \sim \begin{cases} (x^{-2}-1)^{-1/4}\left(A\mathrm{e}^{a\int_x^1 \sqrt{x^{-2}-1}\,\mathrm{d}x} + B\mathrm{e}^{-a\int_x^1 \sqrt{x^{-2}-1}\,\mathrm{d}x}\right), & x<1 \text{ (evanescent)},\\ (1-x^{-2})^{-1/4}\left(C\mathrm{e}^{\mathrm{i}a\int_1^x \sqrt{1-x^{-2}}\,\mathrm{d}x} + D\mathrm{e}^{-\mathrm{i}a\int_1^x \sqrt{1-x^{-2}}\,\mathrm{d}x}\right), & x>1 \text{ (oscillatory)}, \end{cases} \tag{B.6}$$

where $A, B, C, D \in \mathbb{C}$ are constants. Note that the integral in the evanescent region can be performed analytically and is $-I_1(x)$ as defined by (41); the integral in the oscillatory region is not needed since amplitude not phase is of interest. Since the solution w is continuous through the turning point $x = 1$ (even though (B.6) breaks down), there exist connection formulae relating the constants:

$$C = \mathrm{e}^{\mathrm{i}\pi/4}A + \mathrm{e}^{-\mathrm{i}\pi/4}B, \quad D = \mathrm{e}^{\mathrm{i}\pi/4}B. \tag{B.7}$$

They can be found by comparing WKBJ to large-argument asymptotics of the Airy functions Ai and Bi on either side of the turning point (e.g. comparing 10.4.59 with 10.4.60, and 10.4.63 with 10.4.64, in [1], or using 9.3.91,92 of [30], or the more rigorous presentation of the Gans–Jeffreys formulae in Chapter 11 of [31]). If $A = 0$ (w decaying as x decreases in the evanescent region) then $|C| = |D| = |B|$ giving an amplitude of $2|B|/(1-x^{-2})^{1/4}$ in the oscillatory region. When transformed back such a solution $u(r)$ corresponds to the $J_m(r)$ Bessel function. We match the asymptotic amplitude $\sqrt{2/\pi r}$ at large argument (see 9.2.1 of [1]) to fix $B = \frac{1}{2}$ for all m. Hence the Bessel function has typical size

$$|J_m(r)| \approx \begin{cases} \frac{1}{2}(a^2-r^2)^{-1/4}\mathrm{e}^{I_a(r)}, & r<a,\\ (a^2-r^2)^{-1/4}, & r>a. \end{cases} \tag{B.8}$$

Note that an amplitude is implied here in the oscillatory region $r > a$. Note also that a is defined above (B.5), and $I_a(r) < 0$ for $r < a$. Similarly matching the $H_m^{(1)}(r)$ Hankel function large-argument asymptotic gives $|C| = 1$, $D = 0$, so $|A| = 1$ (which dominates), thus typical size

$$|H_m^{(1)}(r)| \approx \begin{cases} (a^2-r^2)^{-1/4}\mathrm{e}^{-I_a(r)}, & r<a,\\ (a^2-r^2)^{-1/4}, & r>a. \end{cases} \tag{B.9}$$

These formulae have been checked against numerical evaluations of Bessel functions and accurately predict amplitudes or evanescent magnitudes everywhere apart from very close to the turning point $r = a$ where they have a weak algebraic singularity, but still provide an upper bound. Substituting (B.8) and (B.9) into (12) gives the desired (40).

References

[1] M. Abramowitz, I.A. Stegun, Handbook of Mathematical Functions with Formulas, Graphs, and Mathematical Tables, 10th ed., Dover, New York, 1964.

[2] M.T. Ahmed, J.D. Lavers, B.E. Burke, An evaluation of the direct boundary element method and the method of fundamental solutions, IEEE Trans. Magn. 25 (1989) 3001–3006.

[3] A.H. Barnett, Asymptotic rate of quantum ergodicity in chaotic Euclidean billiards, Commun. Pure Appl. Math. 59 (2006) 1457–1488.

[4] A. Bogomolny, Fundamental solutions method for elliptic boundary value problems, SIAM J. Numer. Anal. 22 (4) (1985) 644–669.

[5] D. Colton, R. Kress, Inverse Acoustic and Electromagnetic Scattering Theory, Applied Mathematical Sciences, second ed., vol. 93, Springer-Verlag, Berlin, 1998.

[6] R. Courant, D. Hilbert, Methods of Mathematical Physics, vol. I, Interscience Publishers Inc., New York, NY, 1953.

[7] P.J. Davis, The Schwarz Function and Its Applications, The Carus Mathematical Monographs, No. 17, The Mathematical Association of America, Buffalo, NY, 1974 .

[8] A. Doicu, Y.A. Eremin, T. Wriedt, Acoustic and Electromagnetic Scattering Analysis Using Discrete Sources, Academic Press, San Diego, CA, 2000.

[9] T.A. Driscoll, B. Fornberg, Interpolation in the limit of increasingly flat radial basis functions, Comput. Math. Appl. 43 (2002) 413–422.

[10] R. Ennenbach, H. Niemeyer, The inclusion of Dirichlet eigenvalues with singularity functions, Z. Angew. Math. Mech. 76 (7) (1996) 377–383.

[11] G. Fairweather, A. Karageorghis, The method of fundamental solutions for elliptic boundary value problems, Adv. Comput. Math. 9 (1-2) (1998) 69–95, numerical treatment of boundary integral equations.

[12] P.R. Garabedian, Applications of analytic continuation to the solution of boundary value problems, J. Rational Mech. Anal. 3 (1954) 383–393.
[13] A. Karageorghis, The method of fundamental solutions for the calculation of the eigenvalues of the Helmholtz equation, Appl. Math. Lett. 14 (7) (2001) 837–842.
[14] D. Karkashadze, On status of main singularities in 3D scattering problems, in: Proceedings of VIth International Seminar/Workshop on Direct and Inverse Problems of Electromagnetic and Acoustic Wave Theory (DIPED), Lviv, Ukraine, 2001.
[15] M. Katsurada, A mathematical study of the charge simulation method. II, J. Fac. Sci. Univ. Tokyo Sect. IA Math. 36 (1) (1989) 135–162.
[16] M. Katsurada, Asymptotic error analysis of the charge simulation method in a Jordan region with an analytic boundary, J. Fac. Sci. Univ. Tokyo Sect. IA Math. 37 (3) (1990) 635–657.
[17] M. Katsurada, Charge simulation method using exterior mapping functions, Jpn. J. Ind. Appl. Math. 11 (1) (1994) 47–61.
[18] M. Katsurada, H. Okamoto, A mathematical study of the charge simulation method. I, J. Fac. Sci. Univ. Tokyo Sect. IA Math. 35 (3) (1988) 507–518.
[19] M. Katsurada, H. Okamoto, The collocation points of the fundamental solution method for the potential problem, Comput. Math. Appl. 31 (1) (1996) 123–137.
[20] T. Kitagawa, On the numerical stability of the method of fundamental solution applied to the Dirichlet problem, Jpn. J. Appl. Math. 5 (1) (1988) 123–133.
[21] T. Kitagawa, Asymptotic stability of the fundamental solution method, in: Proceedings of the International Symposium on Computational Mathematics (Matsuyama, 1990), vol. 38, 1991.
[22] J.R. Kuttler, V.G. Sigillito, Bounding eigenvalues of elliptic operators, SIAM J. Math. Anal. 9 (4) (1978) 768–778.
[23] A.G. Kyurkchan, The method of auxiliary currents and sources in wave diffraction problems, Soviet J. Commun. Tech. Electron. 30 (1985) 48–58, translated from Radiotekhn. i Èlektron. 29 (no. 11) (1984) 2129–2139 (Russian).
[24] A.G. Kyurkchan, B.Y. Sternin, V.E. Shatalov, Singularities of continuation of wave fields, Physics – Uspekhi 12 (1996) 1221–1242.
[25] B. Landry, E.J. Heller, Statistical properties of many particle eigenfunctions, J. Phys. A 40 (2007) 9259–9274.
[26] H. Lewy, On the reflection laws of second order differential equations in two independent variables, Bull. Am. Math. Soc. 65 (1959) 37–58.
[27] P.G. Martinsson, V. Rokhlin, A fast direct solver for boundary integral equations in two dimensions, J. Comput. Phys. 205 (2005) 1–23.
[28] R.F. Millar, The analytic continuation of solutions to elliptic boundary value problems in two independent variables, J. Math. Anal. Appl. 76 (2) (1980) 498–515.
[29] R.F. Millar, Singularities and the Rayleigh hypothesis for solutions to the Helmholtz equation, IMA J. Appl. Math. 37 (2) (1986) 155–171.
[30] P. Morse, H. Feshbach, Methods of Theoretical Physics, vol. 2, McGraw-Hill, 1953.
[31] F.W.J. Olver, Asymptotics and Special Functions, Academic Press, New York, 1974.
[32] Y.-S. Smyrlis, A. Karageorghis, Numerical analysis of the MFS for certain harmonic problems, M2AN Math. Model. Numer. Anal. 38 (3) (2004) 495–517.